Acoustically driven arrayed waveguide grating

A. Crespo-Poveda,[1,*] A. Hernández-Mínguez,[2] B. Gargallo,[3] K. Biermann,[2] A. Tahraoui,[2] P. V. Santos,[2] P. Muñoz,[3,4] A. Cantarero,[1] and M. M. de Lima, Jr.[1,5]

[1]*Materials Science Institute, Universitat de València, Valencia, Spain*
[2]*Paul Drude Institute for Solid State Electronics, Berlin, Germany*
[3]*iTEAM Research Institute, Universitat Politècnica de València, Valencia, Spain*
[4]*VLC Photonics S.L., Valencia, Spain*
[5]*Fundació General Universitat de València, Valencia, Spain*
[*]*Antonio.Crespo-Poveda@uv.es*

Abstract: We demonstrate compact tunable phased-array wavelength-division multiplexers driven by surface acoustic waves (SAWs) in the low GHz range. The devices comprise two couplers, which respectively split and combine the optical signal, linked by an array of single-mode waveguides (WGs). Two different layouts are presented, in which multi-mode interference couplers or free propagating regions were separately employed as couplers. The multiplexers operate on five equally distributed wavelength channels, with a spectral separation of 2 nm. A standing SAW modulates the refractive index of the arrayed WGs. Each wavelength component periodically switches paths between the output channel previously asigned by the design and the adjacent channels, at a fixed applied acoustic power. The devices were monolithically fabricated on (Al,Ga)As. A good agreement between theory and experiment is achieved.

References and links

1. K. Bergman, L. P. Carloni, A. Biberman, J. Chan, and G. Hendry, *Photonic network on chip design* (Springer, 2014).
2. J. M. Simmons, *Optical network design and planning* (Springer, 2008).
3. C. Dragone, "An N x N optical multiplexer using a planar arrangement of two star couplers," IEEE Photon. Technol. Lett. **3**, 812–815 (1991).
4. H. Takahashi, O. Kazuhiro, T. Hiroma, and I. Yasuyuki,"Transmission characteristics of arrayed waveguide N X N wavelength multiplexer," J. Lightwave Technol. **13**, 447–455 (1995).
5. M. K. Smit, and C. Van Dam, "PHASAR-based WDM-devices : principles, design and applications," IEEE J. Sel. Top. Quantum Electron. **2**, 236–250 (1996).
6. P. Muñoz, D. Pastor, and J. Capmany, "Modeling and design of arrayed waveguide gratings," J. Lightwave Technol. **20**, 661–674 (2002).
7. Chin-Lin Chen, *Foundations for guided-wave optics* (John Wiley & Sons, 2007).
8. M. R. Paiam and R. I. Macdonald, "Design of phased-array wavelength division multiplexers using multimode interference couplers," Appl. Opt. **36**, 5097–5108 (1997).
9. S. Nakamura, Y. Ueno, and K. Tajima, "Femtosecond switching with semiconductor-optical-amplifier-based symmetric Mach-Zehnder-type all-optical switch," Appl. Phys. Lett. **78**, 3929 (2001).
10. G. A. Wurtz, R. Pollard, G. P. Wiederrecht, D. J. Gosztola, V. A. Podolskiy, and A. V. Zayats, "Designed ultrafast optical nonlinearity in a plasmonic nanorod metamaterial enhanced by nonlocality," Nat. Nanotechnol. **6**, 107–111 (2011).

11. X. Li, H. Xu, X. Xiao, Z. Li, Y. Yu, and J. Yu, "Fast and efficient silicon thermo-optic switching based on reverse breakdown of pn junction," Opt. Lett. **39**, 751–753 (2014).
12. M. Ishii, Y. Hibino, F. Hanawa, H. Nakagome, and K. Kato., "Packaging and environmental stability of thermally controlled arrayed-waveguide grating multiplexer module with thermoelectric device," J. Lightwave Technol. **16**, 258–264 (1998).
13. T. Watanabe, N. Ooba, S. Hayashida, T. Kurihara, and S. Imamura, "Polymeric optical waveguide circuits formed using silicone Resin," J. Lightwave Technol. **16**, 1049–1055 (1998).
14. G. Z. Xiao, P. Zhao, F. G. Sun, Z. G. Lu, Z. Zhang, and C. P. Grover, "Interrogating fiber Bragg grating sensors by thermally scanning a demultiplexer based on arrayed waveguide gratings," Opt. Lett. **29**, 2222–2224 (2004).
15. M. R. Paiam, *Applications of multimode interference couplers in wavelength-division multiplexing* (University of Alberta, 1997).
16. N. S. Lagali, *The generalized Mach-Zehnder interferometer using multimode interference couplers for optical communications networks* (University of Alberta, 2000).
17. R. Stabile, A. Rohit, and K. A. Williams, "Monolithically integrated 8×8 space and wavelength selective cross-connect," J. Lightwave Technol. **32**, 201–207 (2014).
18. K. Nashimoto, D. Kudzuma, and H. Han, "High-speed switching and filtering using PLZT waveguide devices," in OptoElectronics and Communications Conference (OECC), 2010 15th, July 2010, 540–542.
19. M. Hashimoto, H. Asakura, K. Nashimoto, H. Tsuda, and D. Kudzuma, "High-speed wavelength selective operation of PLZT-based arrayed-waveguide grating," Electron. Lett. **48**, 1009–1010 (2012).
20. C. Gorecki, F. Chollet, E. Bonnotte, and H. Kawakatsu, "Silicon-based integrated interferometer with phase modulation driven by surface acoustic waves," Opt. Lett. **22**, 1784–1786 (1997).
21. M. M. de Lima Jr., M. Beck, R. Hey, and P. V. Santos, "Compact Mach-Zehnder acousto-optic modulator," Appl. Phys. Lett. **89**, 121104 (2006).
22. M. Beck, M. M. de Lima, Jr., E. Wiebicke, W. Seidel, R. Hey, and P. V. Santos, "Acousto-optical multiple interference switches," Appl. Phys. Lett. **91**, 061118 (2007).
23. M. Beck, M. M. de Lima, Jr., and P. V. Santos, "Acousto-optical multiple interference devices," J. Appl. Phys. **103**, 014505 (2008).
24. A. Crespo-Poveda, R. Hey, K. Biermann, A. Tahraoui, P. V. Santos, B. Gargallo, P. Muñoz, A. Cantarero, and M. M. de Lima, Jr.,"Synchronized photonic modulators driven by surface acoustic waves," Opt. Express **21**, 21669 (2013).
25. J. C. Capmany, P. Muñoz, M. M. de Lima, Jr., and P. V. Santos, "Tunable AWG device for multiplexing and demultiplexing signals and method for tuning said device," Patent Application WO 2012/152977, May 4, A1 (2012).
26. M. M. de Lima, Jr., and P. V. Santos, "Modulation of photonic structures by surface acoustic waves," Rep. Prog. Phys. **68**, 1639–1701 (2005).
27. N. S. Lagali, M. R. Paiam, and R. I. Macdonald, "Theory of variable-ratio power splitters using multimode interference couplers," IEEE Photon. Technol. Lett. **11**, 665–667 (1999).
28. L. B. Soldano and E. C. M. Pennings, "Optical multi-mode interference devices based on self-imaging: principles and applications," J. Lightwave Technol. **13**, 615–627 (1995).
29. M. T. Hill, X. J. M. Leijtens, G. D. Khoe, and M. K. Smit, "Optimizing imbalance and loss in 2×2 3-dB multimode interference couplers via access waveguide width," J. Lightwave Technol. **21**, 2305–2313 (2003).
30. A detailed description of the calculation procedure for the general case of N arms will be published elsewhere.
31. D. Marcuse, "Length optimization of an S-shaped transition between offset optical waveguides," Appl. Opt. **17**, 763–768 (1978).
32. M. M. de Lima, Jr., F. Alsina, W. Seidel, and P. V. Santos, "Focusing of surface-acoustic-wave fields on (100) GaAs surfaces," J. Appl. Phys. **94**, 7848 (2003).

1. Introduction

Wavelength multiplexers and demultiplexers are key components in wavelength-division multiplexing (WDM) technology. Multiplexers enable the combination of different wavelength channels into a WDM signal transmitted through high-capacity optical fibers. The received WDM signal can be separated using an inverse device (demultiplexer) which splits the incoming signal into its constituting wavelength channels. Integrated multiplexers and demultiplexers are commonly based on phased-array WDM technology. In these devices, wavelength dispersion is provided by an array of waveguides (WGs), with length calculated so that constructive interference is granted at each output WG for a different wavelength [1–8]. By applying a phase shift to the arms, a dynamic allocation of the channels can be accomplished, giving rise to new functionalities. The external control of light propagation inside the device allows also for size

reduction, consequently favouring the integration.

An interesting proposal to modify the refractive index of the arms exploits non-linear optical effects [9] to achieve very fast devices operating in the GHz range, at the expense of very long interaction paths to compensate for the weak non-linearities. This obstacle has been recently overcome with the application of plasmonic nanorod metamaterials [10], accomplishing very short time responses and ultra-compact devices. However, the growing and assembly of these materials into conventional photonic circuits can be very challenging. As an alternative, some approaches make use of the thermo-optic effect [11] to control the propagation of the light in the structures, at the cost of a longer time response and operation in the best case in the low MHz range. The thermal inertia prevents the effective index changes from being almost instantaneous, and the diffusion of heat may prevent a precise control of the optical properties in some structures. Fine control of the temperature of the device by means of Peltiers has been used to tune phased-array WDM devices [12–14] with dimensions of the order of tents of mm and very low time responses (in the best case in the order of ~ 2 ms). Thermo-optical phased-array WDM devices with individual addressing of each WGs have also been proposed [15, 16]. A further strategy, widely used nowadays, makes use of electric fields to control the response of the devices by means of the electro-optic effect [17]. Although this approach leads to very fast devices, the addressing of the individual areas in which the refractive index needs to be tuned becomes more demanding as the complexity of the devices increases. In particular, electro-optically tunable phased-array WDM devices with a switching time of tents of ns and active region of several mm have also been reported [18, 19].

Another method, first proposed by C. Gorecki *et al.* [20], and lately generalized by M. M. de Lima *et al.* [21], and M. Beck *et al.* [22, 23], consists of using a surface acoustic wave (SAW) to modulate single or multiple ridge or slot WGs through the acousto-optical effect, with the possibility of adressing several devices with the same SAW beam. This method presents an excellent compromise between speed and size, and can be implemented in almost any material platform such as Silicon, (In,Ga)P or $LiNbO_3$, with processing steps easily implemented using planar semiconductor technology. Moreover, it can be used as a building block for more complex photonic functionalities, such as multiple output waveguides modulators.

In this work, we present two architectures for a compact tunable phased-array wavelength-division multiplexer driven by SAWs in the low GHz range on (Al,Ga)As technology with a SAW-light interaction length of $\sim 120\,\mu$m. One layout uses free propagating regions (FPRs) [3–7] as power splitters and combiners [8], while multi-mode interference (MMI) couplers are employed in the other layout. A dynamic allocation of the different wavelengths channels can be accomplished by adjusting the applied acoustic power. This is in contrast with most of the previous works, which explored colorless designs with a single output [21–23] or, very recently, two outputs [24]. The integration of an acoustically tuned phased-array wavelength-division multiplexer into more complex photonic circuits enables various applications of interest. Moreover, the very short time response makes feasible applications such as a multi-resolution optical spectrum analyzer, a digital signal demultiplexer, or a digital channel exchanger [25]. The layout of the devices can be seen in Fig. 1.

2. Device concept

The devices consist of a phased-array wavelength division multiplexer with multiple access WGs, in which the arrayed WGs are arranged to enable tuning of the device by a standing SAW. The two most used phased-array wavelength division multiplexers designs were considered, in which FPRs and MMI couplers were alternatively used to split and combine the optical signal. The operation principle is similar in both devices. The most common phased-array wavelength multiplexers are built upon two FPRs with the same focal length where light diffracts, linked

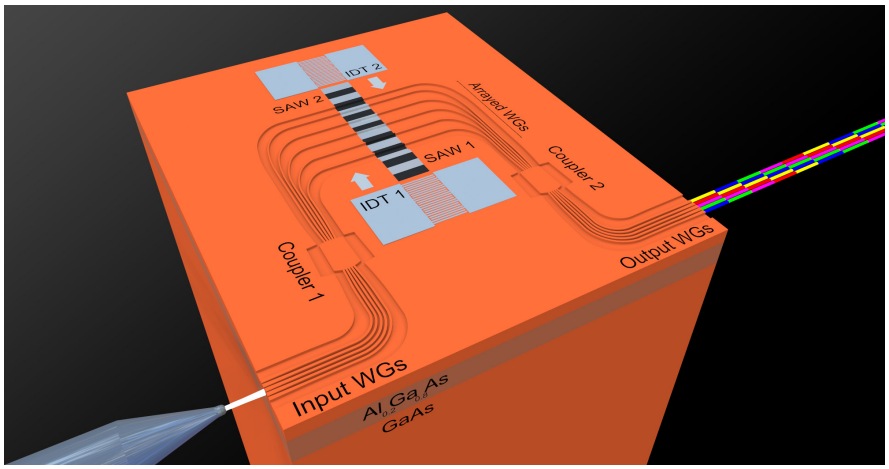

Fig. 1. Illustration (not to scale) of the acoustically driven wavelength-division multiplexers, fabricated on (Al,Ga)As. The light is coupled into an input channel (Input WGs) by means of a optical fibre probe. The passive components consist of a splitter and combiner couplers (Coupler 1 and Coupler 2, respectively) linked by an array of single-mode waveguides (Arrayed WGs). These arrayed WGs are modulated by a standing surface acoustic wave (SAW) generated by two interdigital transducers (IDTs), that dynamically modifies the output channel corresponding to a given optical wavelength.

by an array of single-mode WGs [3–7]. The optical length of each arrayed WG linearly increases by a fixed amount with respect to the preceding WG, causing a wavelength-dependent phase change, which varies linearly along the output plane of the arrayed WGs. As a result, constructive interference will occur for different wavelengths at different points along the focal plane of the second FPR, where the output WGs are placed. As the phase change varies linearly, neighboring wavelength channels will therefore be selected by adjacent output WGs. MMI-based devices are built upon two MMI couplers with the same coupling length. The first coupler is a balanced splitting ratio MMI coupler which divides the incoming light from any of the five access WGs into five identical optical beams. The light is then distributed to the array of single-mode WGs with different relative lengths, which introduce phase delays proportional to the relative length difference. The second MMI coupler combines the delayed optical fields into the output WGs where interference occurs. Due to the phase properties of MMI couplers, the lengths of adjacent array arms are not related in a linear manner [8]. Consequently, neighboring wavelength channels will not necessarily be selected by adjacent WGs, in contrast to FPRs-based devices.

In our approach, the preset output distribution (i.e. the passive distribution operating in the absence of a SAW), which is established by the design of the devices, becomes modified during operation through the variations in the refractive index of the arrayed WGs induced by the SAW. If a proper phase difference between the arrayed WGs $\Delta\Phi = \delta\Phi_{j'} - \delta\Phi_{j}$ (where j' and j refer to the arm numbering) is introduced, a wavelength component can be redirected from its preset output WG to another one. The phase difference $\delta\Phi_{j}$ arises from the SAW modulation via the acousto-optic and the electro-optic effects, associated with the strain and piezoelectric fields, respectively. However, the acousto-optic effect dominates in the situation we discuss here. The magnitude of the phase change introduced by a SAW in the active region can be expressed as [21]:

$$|\delta\Phi| = (2\pi\ell/\lambda)|\delta n_{eff}| = a_p\sqrt{P_{IDT}} \tag{1}$$

where ℓ is the interaction length between the light and the acoustic field, determined by the SAW beam width, λ is the light wavelength, a_p is a proportionality constant that depends on the elasto-optical properties of the material as well as on the overlap between the optical and acoustic fields in the arrayed WGs [26], P_{IDT} is the nominal radio-frequency (RF) power applied to the interdigital transducer (IDT), and $|\delta n_{eff}|$ is the amplitude in the effective index modulation induced by the SAW. The latter is related to the effective index of the jth arm at a given time (t) by:

$$n_{eff(j)} = n_{eff}^0 + \kappa_j|\delta n_{eff}|\cos(\omega_{SAW}t) \tag{2}$$

where n_{eff}^0 is the unperturbed effective refractive index of the fundamental mode in the arrayed WGs, ω_{SAW} is the SAW angular frequency, and $-1 \leq \kappa_j \leq 1$ are weigth factors that account for the amplitude and the phase of the modulation in the jth array arm by a standing SAW perpendicular to the array arms, which is generated by two interdigital transducers (IDTs).

3. Design and simulations

3.1. SAW-driven FPRs-based phased-array WDM device

A conventional FPRs-based WDM device layout has been considered as a starting point, where additional straight sections of the same length (ℓ_e) have been included in the design to accommodate the propagation of the SAWs. In these devices, the arrayed WGs are positioned over a circumference of radius L_f, defined as the focal length of the FPRs, whose center is located in the central access WG of the couplers. The rest of access WGs are positioned following a Rowland circle geometry [4–6]. The length of the arrayed arms linearly increases by an amount $\Delta\ell$ between arms, which is an integer multiple of the optical design wavelength, λ_0, measured inside the array arms. This length difference is chosen in such a way that the phase difference between two neighboring WGs at λ_0 equals an integer multiple of 2π. The linearly increasing length of the arrayed WGs causes the phase deviation associated to the change in the frequency to vary linearly along the array apertures. The focal point of the light will, therefore, also be linearly shifted with the changes in the wavelength in such a way that each pass frequency is focused to the focal plane of the arrayed WGs at distinct points. By placing WGs at the proper positions along the image plane of the arrayed WGs, the different wavelength components can be spatially separated [3–7]. The length of each array arm j, ℓ_j, can be expressed as [7]:

$$\ell_j = \ell_m + \Delta\ell(j-1) \qquad \text{for } j = 1,\ldots,N \tag{3}$$

where ℓ_m is the length of the shortest arm in the array corresponding to $j = 1$, and $\Delta\ell = \left(m\lambda_0/n_{eff}^0\right)$ is the introduced length difference, with m an integer parameter called grating order, λ_0 the design wavelength of the device, and n_{eff}^0 the unperturbed effective refractive index of the fundamental mode in the arms for λ_0. The grating order m is a key parameter that determines the transmission properties of the devices. It characterizes the spacing between two consecutive intensity maxima for the pass wavelengths, which is called the free spectral range (FSR). Adding up the phases due to the propagation in the output FPR and the arrayed WGs, the phase match condition at the output of the device can be expressed as [4, 5, 7]:

$$\frac{2\pi}{\lambda}\left(n_{eff}\Delta\ell + n_r d\sin\theta\right) = 2n\pi \tag{4}$$

where n is an integer, n_r is the effective refractive index in the FPRs, d the arrayed WGs spacing, θ is the dispersion angle in the output FPR, and n_{eff} is the effective refractive index in the array

arms. If Eq. (4) is satisfied, a maximum in the transmission will occur at a wavelength channel λ for a dispersion angle θ. By placing the receiver WGs at the proper positions that meet θ in the output plane of the device, a spatial separation of the different wavelength channels can be achieved. Approximating $\sin\theta \simeq \theta$, we obtain (after some manipulation) [7]:

$$\theta(\lambda) \simeq \left(\frac{n_{eff}\Delta\ell}{n_r d}\right)\left[\left(\frac{\lambda}{\lambda_0}\right)\left(\frac{n_{eff}^0}{n_{eff}}\right)-1\right] \tag{5}$$

which completely determines the dispersion angle for each wavelength λ at the output FPR. At the design wavelength, λ_0, the transmission through the device will show a peak for $\theta(\lambda_0) = 0^\circ$. For λ different from λ_0, the maximum transmission will be shifted by a non-zero angle $\theta(\lambda)$.

A dynamic allocation of the wavelength channels requires the acoustic modulation to introduce additional optical phases in the arrayed WGs, so that for a given input channel, a wavelength component λ is continuously shifted from the preset channel to the rest of the output channels. This additional acoustic phase difference will cause a continuous linear change of the dispersion angle θ along the focusing plane of the output FPR during a SAW period. This means that the phase-match condition given by Eq. (4) must include now an additional term that accounts for the acoustic phase difference between adjacent arrayed WGs:

$$\frac{2\pi}{\lambda}\left[n_{eff}\Delta\ell + n_r d\sin\theta + \left(\kappa_{j+1}-\kappa_j\right)|\delta n_{eff}|\,\ell_e\cos\left(\omega_{SAW}t\right)\right] = 2n\pi \tag{6}$$

where δn_{eff} is the effective refractive index change induced by the SAWs, κ_{j+1} and κ_j are the modulation weights of the arrayed WGs $j+1$ and j as given by Eq. (2), respectively, ω_{SAW} is the SAW angular frequency, t is the time, and ℓ_e is the length of the modulated sections in the arrayed WGs, as defined above. Making the same assumptions as in Eq. (4), we obtain:

$$\theta_{SAW}(\lambda) \simeq \left(\frac{n_{eff}\Delta\ell}{n_r d}\right)\left[\left(\frac{\lambda}{\lambda_0}\right)\left(\frac{n_{eff}^0}{n_{eff}}\right)-1\right] + \delta\theta_{SAW}(\lambda) \tag{7}$$

where an additional term, $\delta\theta_{SAW}(\lambda) = -\left(\ell_e/2n_r d\right)\left(\kappa_{j+1}-\kappa_j\right)|\delta n_{eff}|\cos\left(\omega_{SAW}t\right)$, related to the effects of the acousto-optical modulation appears. Considering Eq. (5), we can rewritte Eq. (7) as:

$$\theta_{SAW}(\lambda) = \theta(\lambda) + \delta\theta_{SAW}(\lambda) \tag{8}$$

If $\delta n_{eff} = 0$, then $\theta_{SAW}(\lambda) = \theta(\lambda)$ as in the preset configuration. When $|\delta n_{eff}|$ increases, $\theta_{SAW}(\lambda)$ differs from the preset value $\theta(\lambda)$ by an amount $\delta\theta_{SAW}$. Defining $\Delta\lambda$ as the spectral separation between wavelength channels, if the applied effective refractive index is sufficient, the wavelength channel selected by output k, λ_k, will be alternatively delivered to the adjacent output channels $(k\pm1)$ which select the preset wavelength channels $\lambda_{k\pm1} = \lambda_k \pm \Delta\lambda$, at different instants along each SAW period. If $|\delta n_{eff}|$ is increased even more, the focus of λ_k will be periodically tilted along the focusing plane of the output FPR to outer receiving WGs.

As the wavelength dispersion in the focal plane of the output FPR is defined by the constant gradient of the optical length within the arrayed WGs, the reconfiguration of the device to switch a particular wavelength from his passive output port to an adjacent one requires a change in the gradient with the corresponding dispersion variation that amounts the spectral separation of two adjacent output channels. We can infer from Eq. (6) that the modulation weights must meet $\kappa_N - \kappa_{N-1} = \ldots = \kappa_{j+1} - \kappa_j = \ldots = \kappa_{m+1} - \kappa_m$, where κ_N and κ_m are, respectively, the modulation weights of the longest and shortest arrayed WGs. Thus, for the FPR-based devices, the difference between the modulations weights, as given by Eq. (2), of two adjacent arrayed WGs is a constant given by $\kappa_{j+1} - \kappa_j = 2/(N-1)$, where N is the number of WGs in the array. Therefore, the separation between the arms in the array with respect to the SAW nodes

and antinodes, which completely determines the $\langle \kappa_j \rangle$, is the key point that enables a proper acoustic tuning. The devices can only be properly tuned if the acoustic phase difference [as determined by Eq. (1)] introduced by the acoustic modulation increases linearly between adjacent WGs. Special care has been taken to design the devices in order to match the WGs separation to the required SAW phase, ensuring that the optical phase match conditions are also satisfied. This imposes no restrictions on the chosen FSR, as the periodic nature of the SAWs allows for placing the WGs at distinct periods of the acoustic wave so that in each case, both the optical and acoustic constraints are simultaneously fulfilled. The particular devices that have been designed and measured contained an array of five arms ($N = 5$), requiring a set of $\langle \kappa_j \rangle$ given by $\langle \kappa_1, \kappa_2, \kappa_3, \kappa_4, \kappa_5 \rangle = \langle \mp 1, \mp 1/2, 0, \pm 1/2, \pm 1 \rangle$. Figure 2(a) shows the actual WGs separation with respect to the standing SAW in the fabricated devices. The layout of the devices can be seen in Fig. 2(b). The optimum imaging condition is achieved by increasing the number of WGs in the array. In the fabricated devices, the width of the arrayed WGs is close to $\lambda_{SAW}/6$, with $\lambda_{SAW} = 5.6\ \mu$m being the SAW wavelength. In general, SAW-driven devices with a larger number of WGs are feasible at the cost of increasing λ_{SAW}, which results in a slower time response, in order to keep the refractive index modulation approximately constant along each WG.

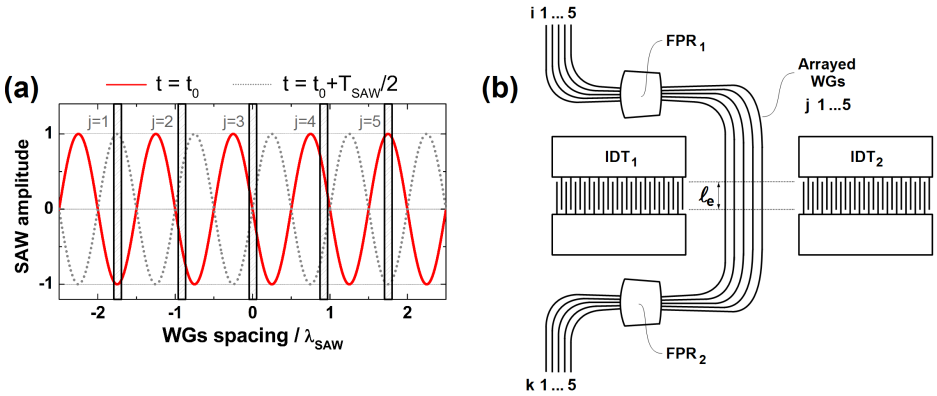

Fig. 2. Relative WG spacings with respect to the standing SAW nodes and anti-nodes, depicted at two different instants along the SAW beating period for the fabricated five WGs FPRs-based WDM device, where $\langle \kappa_1, ..., \kappa_5 \rangle = \langle \mp 1, \mp 1/2, 0, \pm 1/2, \pm 1 \rangle$. The vertical black boxes indicate the WGs positions. (b) Layout of the devices, where the reference WG is the first arm ($m = 1$). In this configuration, the arrayed WGs bend through 180°, resulting in very compact devices.

3.2. SAW-driven MMIs-based phased-array WDM device

In a MMI coupler, within the multimode guiding region, single or multiple images of the input field are formed at different positions perpendicular to the light propagation direction. Different splitting ratios can be accomplished by an appropriated choice of the input WG position, the input field profile, and the coupling length [8, 28, 29]. The latter, without restrictions on the modal excitation, can be theoretically calculated using the following equation [8, 28]:

$$L_c = \frac{P}{N}(3L_\pi) \tag{9}$$

with $P \geq 1$ and $N \geq 1$ integers without common divisor (the shortest devices are obtained taking $P = 1$), and L_π the beat length of the two lowest order modes of the MMI coupler [8, 27, 28].

Following the analysis presented in [8], the length difference between the array arms j, and the reference arm $j = m$ can be roughly estimated by several sets of integer array arm factors. It is therefore important to search for the optimum set, which minimizes the dimensions of the device, and ensures the best possible spectral response. After that, small corrections to the calculated lengths are needed to offset the small phase variations of the transfer phases in the MMI couplers, so that the phase match conditions are satisfied at each output of the device for a given λ. Thus, we can define a new set of non-integer array arm factors, $\langle \alpha_j \rangle$, which exactly satisfy:

$$\frac{2\pi}{\lambda}\left[n_{eff}^{0}\left(\ell_j - \ell_m\right) - n_{eff}^{0}\alpha_j \Delta\ell\right] = 2n\pi \qquad \text{for } j = 1, \ldots, N \tag{10}$$

where n_{eff}^{0} is, as defined before, the effective refractive index of the fundamental mode propagating in the arrayed arms, λ is the light wavelength, ℓ_j is the length of the array arm j, ℓ_m is the length of the shortest arm, $j = m$, α_j are, as defined above, the array arm factors, and $\Delta\ell$ corresponds to the length difference that induces a phase shift of $2\pi/N$ between two adjacent wavelength channels.

A crucial point regarding the SAW modulation of MMI couplers is that, on one hand, *N* images of the input optical field will be obtained with equal spacing $W_{eff,0}/N$, where $W_{eff,0}$ is the effective width of the fundamental mode of the light propagating in the MMI couplers, at the coupling length L_c. On the other hand, the correct positioning of each of the phased arrayed WGs within the standing SAW profile obliges an unequal spacing separation of the WGs for $N > 3$. The values of the coefficients $\langle \kappa_j \rangle$ in Eq. (2) are determined by the relative spatial separation between the modulated WGs, since each WG will experience an acoustic phase and amplitude determined by their position with respect to the maxima and nodes of the standing SAW. Therefore, the calculation of the phase-match conditions have also to take into account the phase-shifts introduced by curved structures required to bring the WGs from the equal spacing separation at the exit of the MMI couplers to the separation that provides the necessary $\langle \kappa_j \rangle$ coefficients. This can be accomplished by considering the lengths of the different arms in the array as the sum of a straight and a curved length:

$$\frac{2\pi}{\lambda}\left[n_{eff}^{0}\left(\ell_j - \ell_{s_j}\right) - n_{eff}^{c}(R)\,\ell_{c_j}\right] = 2n\pi \qquad \text{for } j = 1, \ldots, N \tag{11}$$

where ℓ_{s_j} and ℓ_{c_j} are the length of the straight and curved WG sections, respectively, of the arrayed arm j, and $n_{eff}^{c}(R)$ is the effective refractive index of the fundamental mode propagating in the curved sections of the arrayed arms. For very large radii of curvature, we can approximate $n_{eff}^{c}(R \to \infty) \cong n_{eff}^{0}$ with good results.

In the actual device designed as a proof of concepts, 5×5 MMI couplers connected by a phased array of 5 waveguides were employed ($N = 5$). Therefore, the whole device has 5 possible inputs with 5 different outputs. In passive operation, depending on the input used, each of the output WGs delivers a different wavelength denoted by $\lambda_{p+1} = \lambda_p + \Delta\lambda$, where $\Delta\lambda$ is the device spectral separation. The different channels are denoted by $\langle \lambda_{-2}, \lambda_{-1}, \lambda_0, \lambda_1, \lambda_2 \rangle$, with λ_0 the design wavelength. Thus, an output WG k is connected to different input WGs i through different wavelengths. Due to the spectral properties of MMI couplers, adjacent WG channels do not correspond to spectrally contiguous outputs [8]. The complete set of wavelength assignment possibilities is given in Table 1 (upper panel).

An active reconfiguration of the MMI-based WDM device requires the acoustic modulation to dynamically introduce optical phases in the arrayed arms [the set of κ_j in Eq. (2)] so that for a given input channel the passive spectral distribution in the outputs is switched to another, corresponding to any of the responses expected to different inputs. Owing to the nature of the transfer phases between the access ports in the case of MMI couplers [8], the values of κ_j for the

Table 1. Wavelength assignment of a five-channel MMI-phasar multiplexer calculated for $\mathbb{S}^{'}$ and $\mathbb{S}^{''}$ taking m = 1 as the reference arm, for the passive device (upper table), and different values of Λ. The same wavelength assignment is obtained for both sets of solutions, incrementing the effective index change by a different Λ.

$\mathbb{S}'(\Lambda=0)=\mathbb{S}''(\Lambda=0)$	Output (k)				
Input (i)	**1**	**2**	**3**	**4**	**5**
1	λ_0	λ_{-2}	λ_2	λ_1	λ_{-1}
2	λ_{-2}	λ_1	λ_0	λ_{-1}	λ_2
3	λ_2	λ_0	λ_{-1}	λ_{-2}	λ_1
4	λ_1	λ_{-1}	λ_{-2}	λ_2	λ_0
5	λ_{-1}	λ_2	λ_1	λ_0	λ_{-2}

$\mathbb{S}'(\Lambda=-2)=\mathbb{S}''(\Lambda=-1)$	Output (k)				
Input (i)	**1**	**2**	**3**	**4**	**5**
1	λ_1	λ_{-1}	λ_{-2}	λ_2	λ_0
2	λ_{-1}	λ_2	λ_1	λ_0	λ_{-2}
3	λ_{-2}	λ_1	λ_0	λ_{-1}	λ_2
4	λ_2	λ_0	λ_{-1}	λ_{-2}	λ_1
5	λ_0	λ_{-2}	λ_2	λ_1	λ_{-1}

$\mathbb{S}'(\Lambda=-1)=\mathbb{S}''(\Lambda=2)$	Output (k)				
Input (i)	**1**	**2**	**3**	**4**	**5**
1	λ_{-2}	λ_1	λ_0	λ_{-1}	λ_2
2	λ_1	λ_{-1}	λ_{-2}	λ_2	λ_0
3	λ_0	λ_{-2}	λ_2	λ_1	λ_{-1}
4	λ_{-1}	λ_2	λ_1	λ_0	λ_{-2}
5	λ_2	λ_0	λ_{-1}	λ_{-2}	λ_1

$\mathbb{S}'(\Lambda=1)=\mathbb{S}''(\Lambda=-2)$	Output (k)				
Input (i)	**1**	**2**	**3**	**4**	**5**
1	λ_2	λ_0	λ_{-1}	λ_{-2}	λ_1
2	λ_0	λ_{-2}	λ_2	λ_1	λ_{-1}
3	λ_{-1}	λ_2	λ_1	λ_0	λ_{-2}
4	λ_{-2}	λ_1	λ_0	λ_{-1}	λ_2
5	λ_1	λ_{-1}	λ_{-2}	λ_2	λ_0

$\mathbb{S}'(\Lambda=2)=\mathbb{S}''(\Lambda=1)$	Output (k)				
Input (i)	**1**	**2**	**3**	**4**	**5**
1	λ_{-1}	λ_2	λ_1	λ_0	λ_{-2}
2	λ_2	λ_0	λ_{-1}	λ_{-2}	λ_1
3	λ_1	λ_{-1}	λ_{-2}	λ_2	λ_0
4	λ_0	λ_{-2}	λ_2	λ_1	λ_{-1}
5	λ_{-2}	λ_1	λ_0	λ_{-1}	λ_2

reconfiguration satisfying the phase-match conditions at the output channels are more complex than in the FPRs-based devices [30]. In this way, there are a total of 20 different solutions for the combination of $\langle \kappa_j \rangle$ that can possibly be used for the reconfiguration of the devices in the case of 5 arms. Table 2 shows half of the different sets $\langle \kappa_j \rangle$ that satisfy this condition (the other half are trivially obtained by multiplying the coefficients by -1). They have been arranged in two major groups named $\mathbb{S}^{'}$ and $\mathbb{S}^{''}$, corresponding to solutions that provide the same channel reconfiguration result for a given δn_{eff}. Indeed, by substituting $\delta n_{eff} = \Lambda \delta n_{eff}^{min}$ ($\Lambda \in \mathbb{Z}$) in Eq. (2), where δn_{eff}^{min} is the minimum effective index change needed to reconfigure the output from the preset configuration to another one, it is easy to see that switching from one main set of solutions to the other corresponds to incrementing δn_{eff} by a different integer multiple. Thus, the same wavelength assignment can be obtained for both $\mathbb{S}^{'}$ and $\mathbb{S}^{''}$, for applied effective index changes differing by an integer multiple. The connection between both sets of solutions is fully described in Table 1. As the devices are fully bidirectional, it should be noted that, in general, $\mathbb{S}_j \equiv \mathbb{S}_{N+1-j}$. In this work, the characterized devices were fabricated to operate with SAW nodes at the central array arm (solutions $\mathbb{S}_3^{'}$ and $\mathbb{S}_3^{''}$ in Table 2). Figure 3(a) shows the arrayed arms distribution with respect to the standing SAW for a fabricated device (solution $\mathbb{S}_3^{''}$), depicted at two different instants along the standing SAW period. The SAW node is placed at the center WG, and the anti-nodes at the outer WGs. The nodes remain fixed during the SAW beating, whereas the SAW amplitude at the anti-nodes continuously oscillates up to the

maximum value with opposite phases. The result is a varying refractive index modulation in the arrayed WGs which enables the complete dynamic allocation of the wavelength channels when the proper acoustic power is applied. Due to the periodic nature of the SAWs, the arrayed WGs can be placed at distinct periods of the acoustic wave, simultaneously meeting the optical and the acoustic constraints.

In the fabricated devices, the arrayed WGs are placed at the appropriated acoustic positions by means of large radius S-bend WGs, minimizing the width of the MMI couplers, and, consequently, the dimensions of the device. This also ensures that each of the arrayed WGs suffers a change in the effective refractive index of appropriated magnitude and phase, maximizing therefore the acousto-optical modulation without introducing undesirable phase changes. Moreover,

Table 2. Calculated array arm factors, $\langle \kappa_j \rangle$, for a 5×5 device. The different $\langle \kappa_j \rangle$ can be classified into two main sets, $\mathbb{S}^{'}$ and $\mathbb{S}^{''}$. The numbering of the different sets indicates the position of the acoustic node in the $\langle \kappa_j \rangle$.

	Arm weight factor (κ_j)				
Solutions	κ_1	κ_2	κ_3	κ_4	κ_5
$\mathbb{S}^{'}_1$	0	$-1/2$	$1/2$	-1	1
$\mathbb{S}^{'}_2$	$1/2$	0	1	$-1/2$	-1
$\mathbb{S}^{'}_3$	$-1/2$	-1	0	1	$1/2$
$\mathbb{S}^{'}_4$	1	$1/2$	-1	0	$-1/2$
$\mathbb{S}^{'}_5$	-1	1	$-1/2$	$1/2$	0
$\mathbb{S}^{''}_1$	0	-1	1	$1/2$	$-1/2$
$\mathbb{S}^{''}_2$	1	0	$-1/2$	-1	$1/2$
$\mathbb{S}^{''}_3$	-1	$1/2$	0	$-1/2$	1
$\mathbb{S}^{''}_4$	$-1/2$	1	$1/2$	0	-1
$\mathbb{S}^{''}_5$	$1/2$	$-1/2$	-1	1	0

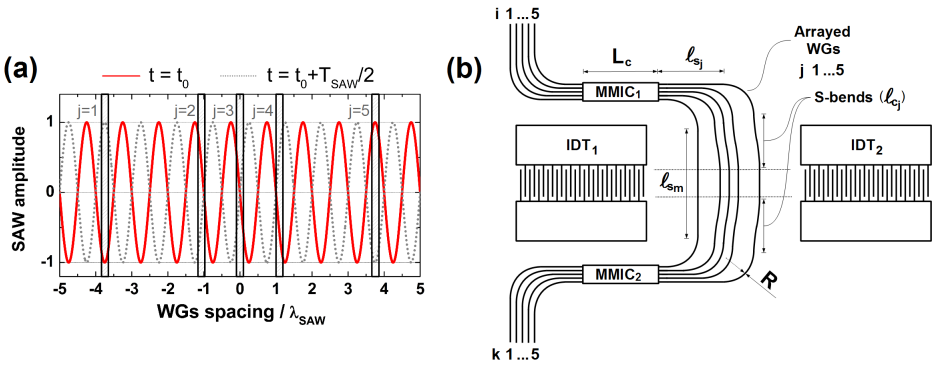

Fig. 3. (a) Relative waveguide spacings with respect to the standing SAW nodes and antinodes, depicted at two different instants along the SAW beating period for the fabricated five WGs MMIs-based devices, corresponding to solution $\mathbb{S}^{''}_3$. The vertical black boxes indicate the WGs positions. (b) Layout of the fabricated acoustically driven MMIs-based phased-array WDM devices, where the reference WG is the first arm (m = 1).

the radius of curvature of the S-bends is infinite at the endpoints, so they can be very effectively linked to the straight WGs avoiding transition losses [31]. Figure 3(b) shows a simplified drawing of one of the fabricated devices. The optical length difference for each of the phased-array arms comes from the S-bends, together with straight WGs of length ℓ_{s_j}, placed at the ending section of the access output and input ports of the splitter and combiner MMI couplers, respectively. To simplify the design, these straight WGs are connected to the S-bends in the array arms using arc bends with the same radii of curvature. Straight WG sections with the same length are used to connect the S-bends coming from the MMI couplers, defining the modulated region of the device. The IDTs are situated at both sides of the arrayed WGs, so that the SAWs reach the active region perpendicularly. For further simplicity, the reference arrayed arm of the multiplexer only comprises two arc bends and a straight WG section of length ℓ_{s_m}. In this configuration, the arrayed WGs bend through 180°, which results in very compact devices.

3.3. Simulated results

An $(\mathrm{Al},\mathrm{Ga})\mathrm{As}$ platform was chosen, as it offers a good compromise between the index contrast in the processed WGs, and its acoustic properties. The structure of the simulated WGs is shown in Fig. 4(a), with W and H being the width and etching depth, respectively. The guiding layer consists of a 300-nm-thick GaAs film, which is deposited on a 1500-nm-thick $\mathrm{Al}_{0.2}\mathrm{Ga}_{0.8}\mathrm{As}$ buffer layer. Both layers are grown on a (001) GaAs substrate. Figure 4(b) shows the calculated optical field distribution of the fundamental TE mode for the arrayed WGs, taking $\mathrm{W} = 900$ nm, and $\mathrm{H} = 150$ nm. The simulation shows the very good confinement of the propagating mode for the described WG structure.

Figure 5(a) shows the simulated response of the FPRs-based devices in the absence of SAWs, calculated using a commercial software. The devices were optimized for a design wavelength, λ_0, of 900 nm. Assuming an etching depth, H, of 150 nm, the effective refractive index considered in the calculations were $\mathrm{n}_{\mathrm{eff}}^{900} = 3.4872$ for the FPRs, and $\mathrm{n}_{\mathrm{eff}}^{900} = 3.4669$ for the 900-nm-width arrayed WGs. A maximum imbalance of ~ 2.0 dB is expected between the different output channels, with an average insertion loss of ~ -9.0 dB. It should be noted that adjacent wavelength channels are selected by adjacent output WGs. Figure 5(b) shows the response corresponding to $\mathrm{i} = 3$ when the arrayed WGs are modulated by the SAWs. In the absence of acoustic excitation, the device layout ensures that the design wavelength λ_0 follows the route $(\mathrm{i},\mathrm{k}) = (3,3)$. When the arrayed WGs are modulated by the SAWs, each wavelength channel is dynamically assigned to the adjacent output WGs along the SAW period. The calculated phase difference required to obtain a complete shift in terms of wavelength of one channel is 1.26 rad between adjacent waveguides. The SAW wavefront width corresponds to the IDT length, 120 μm and therefore, the required effective index change in each arrayed waveguide

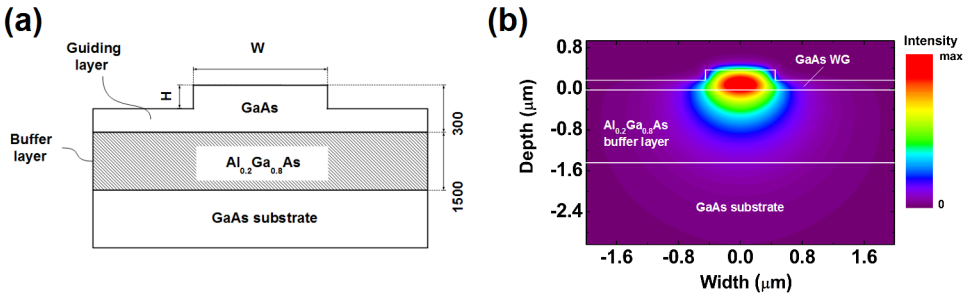

Fig. 4. Structure of the simulated $(\mathrm{Al},\mathrm{Ga})\mathrm{As}$ WGs (a), and simulated optical distribution of the fundamental TE mode, assuming $\mathrm{W} = 900$ nm, and $\mathrm{H} = 150$ nm (b).

is $\{-3.02, -1.51, 0, 1.51, 3.02\} \times 10^{-3}$, for $j = 1, ..., 5$, respectively.

The response of the MMI-based devices was simulated by a guided-mode propagation analysis algorithm [8, 28], which takes into account the phase difference associated to the relative length of the array arms. Assuming a $\approx$ 140-nm-etching depth after the processing of the samples, the effective refractive indices considered in the simulations were $n_{eff}^{910} = 3.4525$, for the 900-nm-width waveguides in the array, and $n_r^{910} = 3.4630$ for the 19-μm-width multimode guiding region, for light with TE polarization, in $(Al, Ga)As$. The effects of the acoustic modulation were included by modifying the effective refractive index according to Eq. (2). Figure 6 shows the simulated results for the MMIs-based WDM device corresponding to solution $\mathbb{S}_3''$. The simulated response of the multiplexer in the absence of acoustic modulation is shown in Fig. 6(a). Figure 6(b) shows the response of the device for the route $(i, k) = (1, 1)$, as a function of the applied effective index change for the different wavelength channels. The design ensures that the design wavelength λ_0 (909 nm) is assigned to the route $(i, k) = (1, 1)$ when no acoustic excitation is applied. The pass wavelength associated to each route (i, k) perfectly matches the previously calculated channel assignment, shown in Table 1 (upper panel).

The calculated insertion losses through the MMI couplers at the pass wavelength are

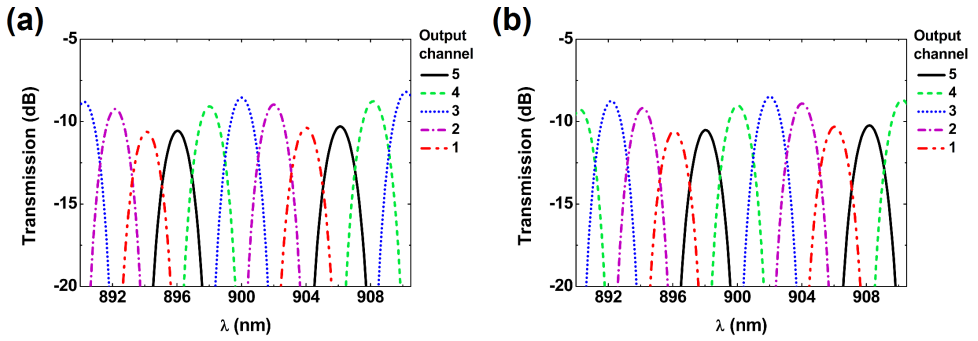

Fig. 5. Simulated results corresponding to the FPRs-based WDM device. (a) Spectral response corresponding to input waveguide $i = 3$. The response associated to other input waveguides has a similar transmission pattern. (b) Spectral response of the device calculated for $i = 3$, introducing a relative phase shift of 1.26 rad between adjacent arrayed WGs.

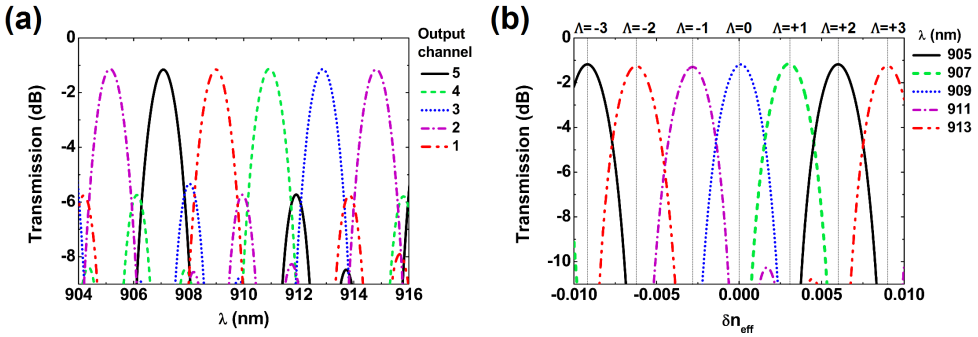

Fig. 6. Simulated results corresponding to the MMIs-based WDM device. (a) Spectral response corresponding to input waveguide $i = m = 1$. The response associated to other input waveguides has a similar transmission pattern. (b) Spectral response of the devices corresponding to $\mathbb{S}_3''$, calculated at the output plane of the device as a function of the applied effective refractive index modulation for the route $(i, k) = (1, 1)$.

~ 1.2 dB, with maximum sidelobe levels of ~ -4.6 dB with respect to the mainlobe maxima. The maximum crosstalk in a 0.5 nm-width region around the pass wavelength is ~ -12 dB, and the window in which the crosstalk is below -20 dB is ~ 0.24 nm wide. Because this low-crosstalk region around the pass wavelength is very narrow, the device properties will in general be very sensitive to the fabrication process. As the acoustic modulation increases, the different wavelengths channels in the multiplexer are also dynamically assigned to other output waveguides. In particular, when the effective refractive index change reaches $\pm\delta n_{eff}^{min} = \pm 3.05 \times 10^{-3}$ (corresponding to $\Lambda = \pm 1$), the output channel ($k = 1$) oscillates from the preset wavelength λ_0 to $\lambda_{\pm 1}$ within a SAW period. If the applied effective refractive index change is increased to $\pm\delta n_{eff} = \pm 2\delta n_{eff}^{min} = \pm\, 6.15 \times 10^{-3}$ (corresponding to $\Lambda = \pm 2$), a complete spectral reconfiguration is accomplished at the output channels, with $k = 1$ oscillating from the preset channel λ_0 to $\lambda_{\pm 1,\pm 2}$ within a SAW period.

4. Sample and device fabrication

The devices were fabricated on a sample grown by molecular beam epitaxy on a (001) GaAs wafer. The sample consists of a 300-nm-thick GaAs film forming the guiding layer, which is deposited on a 1500-nm-thick $Al_{0.2}Ga_{0.8}As$ buffer layer, as stated before. The modulators were fabricated in two steps using contact optical lithography. First, Ti/Al/Ti IDTs were fabricated using a lift-off process in a split-finger configuration for efficient SAW generation. The IDTs were designed for a SAW wavelength of $\lambda_{SAW} = 5.6\ \mu$m [32] (corresponding to a resonance frequency of approximately 520 MHz), with finger width and spacing of 700 nm. A second step of plasma etching was employed to create the $\sim$140-nm-deep grooves delimiting the rib WGs of the devices. The width of the WGs within the active region was 900 nm (approximately $\simeq \lambda/6$), which is narrow enough to ensure a constant acoustic amplitude of modulation through the WG width [21, 22], and sufficient for reliable fabrication using contact optical lithography and etching techniques. The length of the modulated WGs in the active region is 120 μm, as determined by the IDT aperture. Details of the fabricated devices can be seen in the micrographs shown in Fig. (7).

A crucial characteristic in the design of the devices is the separation between the arrayed arms in the modulated region. In the FPRs-based WDM devices, an orthogonal layout was employed, where the positions of the horizontal straight WG sections between the SAW transducer was adjusted to equidistant positions in the sinusoidal SAW. Considering the periodic nature of the SAWs, the separation between adjacent arrayed WGs which exactly matches the optical and acoustical constraints is $D = 6.53\ \mu$m. The dimensions of the devices were optimized to operate around 900 nm, for light with TE polarization. The focal length of the FPRs is 105.305 μm. The incremental length between arrayed WGs is $\Delta\ell = 18.43\ \mu$m for an etching depth of 150 nm and, therefore, the length difference between the longest and the reference arm is $\sim 73.72\ \mu$m. The total size of the fabricated devices including the IDTs is $\sim (4.7 \times 2.7)$ mm^2.

The optimum relative distances between an arrayed WG j and the reference arm m, $D_{(j,m)}$, in the MMI-based devices are $\{D_{(5,1)}, D_{(4,1)}, D_{(3,1)}, D_{(2,1)}\} \simeq \{42.0, 31.7, 21.9, 12.1\}\ \mu$m, and $\simeq \{42.0, 27.1, 21.0, 14.9\}\ \mu$m, for the $\mathbb{S}_3'$ and $\mathbb{S}_3''$ devices, respectively. We determined $\Delta\ell = 19.26\ \mu$m for an etching depth of 150 nm and, therefore, the calculated exact array arm factors, which meet Eq. (10) are $\langle \alpha_1, ..., \alpha_5 \rangle = \langle 0, 1.9975, 2.9813, 4.0416, 5.9817 \rangle$. Accordingly, the length difference between the longest and the reference arm is 115.23 μm. The designed MMI couplers were optimized for the TE polarization, with a width $W = 19\ \mu$m, and a coupling length $L_c = 1158.34\ \mu$m. The width and length of the MMI couplers in the devices were optimized to operate around 910 nm. However, due to the high operational tolerances of these couplers, the working wavelength can be extended over a wide range around the design wavelength with small losses in the transmitted intensity. The calculated excess loss of the

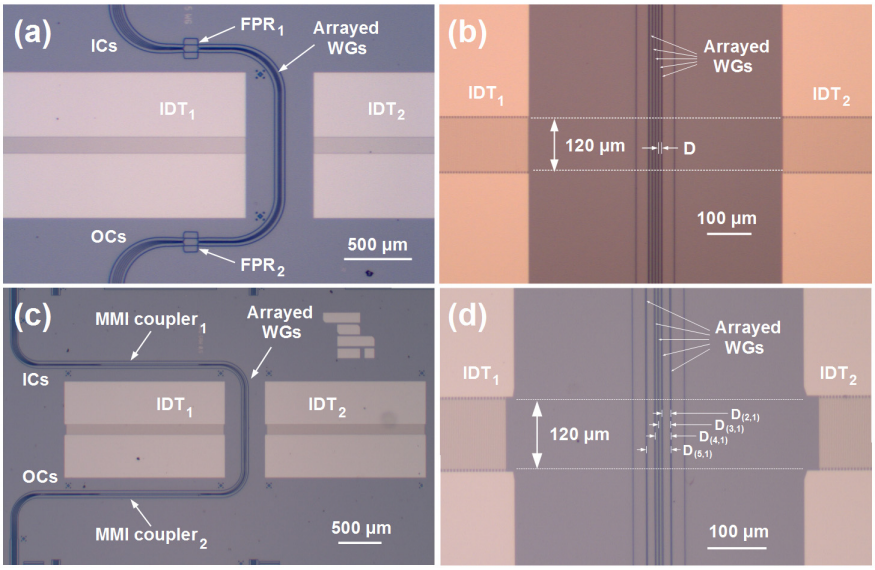

Fig. 7. (a) Top view micrograph of the fabricated FPRs-based WDM device, and detail of the modulated region (b), where D $\simeq 6.53\ \mu$m. (c) Top view micrograph of the fabricated MMIs-based WDM devices corresponding to $\mathbb{S}_3^{'}$, and detail of the modulated region of the multiplexer (d). The values of the different $D_{(j,j')}$ are given in the text.

5×5 MMI coupler was -0.64 dB for λ_0, and the maximum increment in the average excess loss calculated along the FSR was -1.38 dB. The access WGs of both the splitter and combiner MMI couplers are tapered to avoid back-reflections into previous guiding sections of the device. The optimized tapered WGs are 181 μm-long, with 3 μm-width sections connecting the single-mode WGs to the MMI couplers. The input WGs of the devices are also tapered, with a 4 μm-wide initial section to favour the coupling of the light using a lensed optical fiber probe. With an arc bend radius of 300 μm, the total size of the designed devices, including the IDTs, was $\sim (4.7\times3.1)$ mm^2.

5. Experimental setup

Figure 8 shows an overview of the experimental setup for measuring the acoustically driven WDM devices. The device was optically characterized by coupling light into the input WG using a tapered optical fiber probe with a lensed tip. As light source, we used a superluminescent diode (SLD) with peak emission centered at 920 nm, with a full width at half maximum of approximately 40 nm, as well as a tunable Ti:Sapphire laser pumped by a 532 nm diode laser. The fiber probe was mounted on a piezoelectrically controlled X-Y-Z stage to allow for an accurate positioning relative to the input WG edge. The transmitted light was reflected by a right angle mirror facing the cleaved edge of the output WGs, collected by a long working distance $20\times$ objective focused on the device edge, and coupled to a single mode fiber. The objective magnification, in combination with the single mode fiber, enables the spatial selection of the output WG to be measured. The propagation of TE or TM modes was filtered with a linear polarizer (Pol.) placed before a beam splitter (Spl.), in such a way that half of the light was measured by a monochromatic CMOS (Complementary Metal-Oxide Semiconductor) camera to continuously track the coupling, and the other half coupled to the output fiber. The different wavelength channels were spatially separated with a monochromator (Spect.), and the spec-

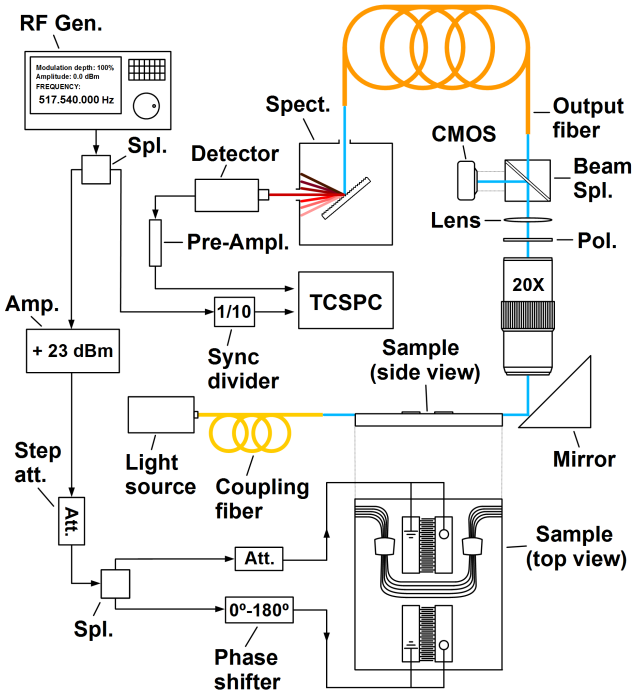

Fig. 8. Diagram showing the setup used to measure the time response of the light transmission through the devices. A 20× objective with focal plane located at the edge of the sample collects the light from the OWGs. A polarizer is used to filter the TE or the TM modes. A single-mode fiber placed at the image plane selects the light from one of the output WGs. The static response of the device was measured using a CCD camera placed after a monochromator (Spec.). The time-resolved traces were recorded using a photomultiplier tube (MCP-PMT) or an avalanche photodiode (APD) synchronized with the RF signal that generates the SAWs. In order to obtain synchronization, the signal from the RF generator (RF gen.) is sent to a splitter (spl.) in a way that 50% of the signal has its frequency divided by 10. This is necessary to keep the trigger within the operational frequency range of the time-correlated single photon counting (TCSPC) module. The other half of the signal goes through a controllable attenuator (Step att.), a fixed-gain amplifier (Ampl.), and then is again split to drive the interdigital transducers. A phase shifter is used to control the relative phase between the IDTs. A second step attenuator is used to compensate for the insertion losses through the phase shifter.

tral response of the device was measured employing a very sensitive CCD (Charged-Coupled Device) camera. The time-resolved measurements were obtained using either a Si avalanche photodiode (APD) with a time resolution of 500 ps, or a micro-channel plate photomultiplier tube (MCP-PMT) with a time resolution of 300 ps. Both detectors were synchronized with the RF signal driving the IDTs. In order to grant synchronization with the detector, the RF signal was first split. One half of the signal passed through a frequency divider in order to match the frequency range requirements of the electronics of the time-correlated single photon counting (TCSPC) module, and then used to trigger the detector. The second half passed through a controllable step attenuator (Step att.) and a fixed gain amplifier (Amp.). The amplified signal was again split, as two IDTs are required to create the standing SAW, and a phase shifter is used to control the relative phase between the SAWs generated by each IDT. This phase control allows a fine tune of the positions of the nodes and the anti-nodes of the standing SAW perpendicularly to the arrayed WGs, optimizing therefore the response of the device.

6. Experimental results

Figure 9(a) shows the measured spectral response of one of the FPRs-based WDM devices, corresponding to input WG $\mathrm{i} = 3$ for light with TE polarization. The losses related to absorption during the propagation through the FPRs and the arc bends are estimated at ~ 12 dB. Figure 9(b) shows the spectral response of one of the designed MMIs-based WDM device for light with TE polarization, measured in the absence of acoustic excitation, for the route $(\mathrm{i},\mathrm{k}) = (1,1)$. Only the results for the TE polarization are shown. With no RF power applied to the IDTs, each wavelength signal is mostly selected by the output WG previously determined by the design of the multiplexer. The response is, in each case, normalized to the transmission of a straight WG. The losses related to absorption during the propagation through the MMI couplers and the arc bends are estimated at ~ 16 dB. The response of the multiplexer is shifted by -1 nm with respect to the previously simulated spectral response, with the design wavelength λ_0 centered at 909 nm. Deviations in the refractive index values of the guiding layers and in the width of the WGs due to the fabrication process result in changes in the effective refractive index of the modes propagating in the array arms. According to simulations, a shift of $\pm$ 1 nm in the calculated spectral response can be expected for a deviation of $\pm$ 0.116% in the effective refractive index of the fundamental mode in the array arms, which is close to the result presented in [8], without increasing the insertion losses. By comparing the simulated results with Fig. 9, a degradation of the measured spectral response with respect to the simulations can be observed. The surface irregularities of the WGs and other defects introduced during the processing of the sample result in additional effective phase shifts in the propagated fields. These additional phases slightly decrease the performance of the devices, resulting in higher crosstalk at the pass wavelengths. Furthermore, the reduced number of arrayed WGs in the FPRs-based devices also contributes to the high crosstalk level we see in Fig. 9(a), and could be significantly improved by placing more WGs in the array.

When the IDTs are excited by a SAW, a dynamic allocation of the wavelength channels is achieved. The power dependence of the time-resolved transmission traces corresponding to the $\mathbb{S}_3^{'}$ MMIs-based WDM device are shown in Fig. 10 for different RF powers ($\mathrm{P_{IDT}}$). The measurements were performed taking $\mathrm{i} = 1$, for light with TE polarization and $\lambda = 916.6$ nm, using an APD. The total transmission is normalized to 1. At very small $\mathrm{P_{IDT}}$ values [Fig. 10(a)], the modulation is negligible, with the preset output WG, $\mathrm{k} = 5$, contributing to nearly 80 % of the total transmission. For $\mathrm{P_{IDT}} = 6.3$ mW [Fig. 10(b)], the modulation becomes clearly visible at the preset channel, $\mathrm{k} = 5$, as a fraction of the optical power is transferred to the channels $\mathrm{k} = 3$ and $\mathrm{k} = 4$. The higher mean value of the trace corresponding to $\mathrm{k} = 4$, with respect to $\mathrm{k} = 3$, can be explained by the higher crosstalk associated to $\mathrm{k} = 4$. Small changes in the tem-

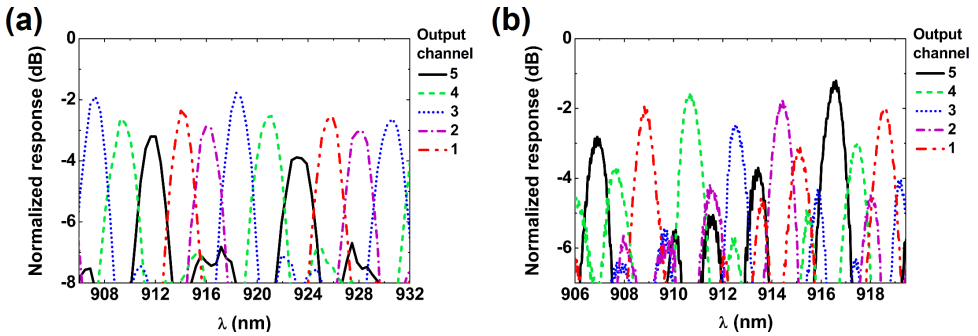

Fig. 9. (a) Measured spectral response of a FPRs-based WDM device corresponding to input waveguide $i = 3$ for light with TE polarization. The measurements are normalized to the transmission of a straight WG. (b) Measured spectral response of a MMIs-based WDM device corresponding to input waveguide $i = m = 1$ for light with TE polarization. The other input channels have similar transmissions.

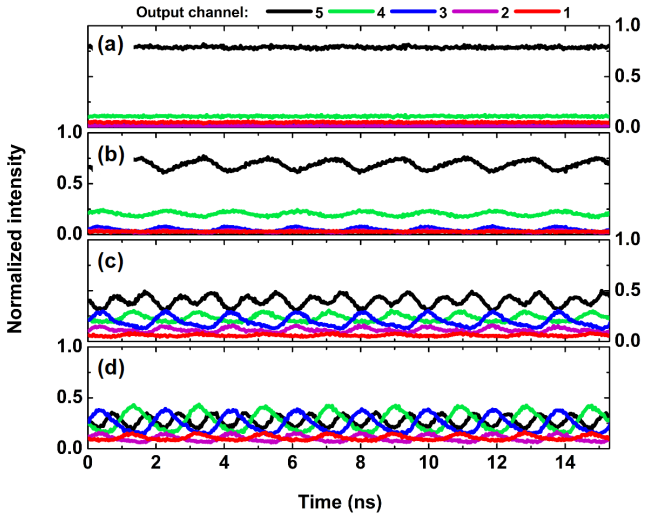

Fig. 10. Time-resolved measurements recorded for the light leaving the OCs of the MMIs-based devices corresponding to $\mathbb{S}_3^{'}$, measured for $\lambda = 916.6$ nm, $i = 1$, and TE polarization. The different traces correspond to RF powers of: (a) $P_{IDT} = 79.4$ nW, (b) $P_{IDT} = 6.3$ mW, (c) $P_{IDT} = 39.8$ mW, and (d) $P_{IDT} = 79.4$ mW on each IDT.

perature owing to the acoustic excitation can also shift the response of the device, displacing the optimum pass wavelength, and therefore, increasing the crosstalk. As P_{IDT} further increases [Figs. 10(c) and (d)], most of the light oscillates among channels 3, 4 and 5, reaching a similar mean value for $P_{IDT} = 79.4$ mW. This situation corresponds to $\Lambda \approx \pm 1$.

The dynamic allocation of the wavelengths in our device can be better observed by improving the time resolution of our experiments. This has been done by replacing the APD detector by a MCP-PMT for conditions close to $\Lambda \approx \pm 1$. Figure 11(a) shows the time-resolved traces recorded for the FPRs-based WDM devices along one acoustic period, measured for $\lambda = 899$ nm, and TE polarization, taking $i = 3$ as the input WG, for a total power of $P_{IDT} \sim 80$ mW on each IDT. The total transmission is normalized to 1. Here, the light oscillates

between the preset channel (k = 3) and the neighbour channels k = 2 and k = 4. Note that the traces for k = 2 and k = 4 are de-phased by 180° with respect to each other. The maximum transmission through each of these channels occurs for the times in which the cosine term in Eq. (2) is either +1 (k = 4) or −1 (k = 2). In contrast, two maxima in the transmission are visible at the preset channel k = 3 corresponding to the times in which the standing SAW vanishes. A negligible modulation is observed at the outer WGs, k = 1 and k = 5. In this way, during a SAW cycle the optical signal oscillates from the preset output channel k = 3 to the two adjacent WGs, k = 2 and k = 4. For comparison, Fig. 11(b) shows the simulated results for the same device, assuming an effective index change of 1.50×10^{-3}, which corresponds approximately to $\Lambda \approx \pm 1$. In addition, Fig. 12(a) shows the time-resolved traces obtained for the $\mathbb{S}_3''$ MMIs-based WDM device for light with TE polarization, taking i = 2, $P_{IDT} \sim 80$ mW on each IDT, and $\lambda = 899$ nm. Again, a single maximum in the transmission can be observed along the SAW period at the lateral channels, k = 2 and k = 4, with a 180°-dephasing synchronization between them. Two maxima are also visible at the preset channel k = 3, between the maxima corresponding to k = 2 and k = 4, respectively. A very weak modulation is observed at the outer channels, k = 1 and k = 5, as expected. Once more the experiments are in very good agreement with the simulations of the same device, assuming $\delta n_{eff} = \pm 2.80 \times 10^{-3}$, shown in Fig. 12(b).

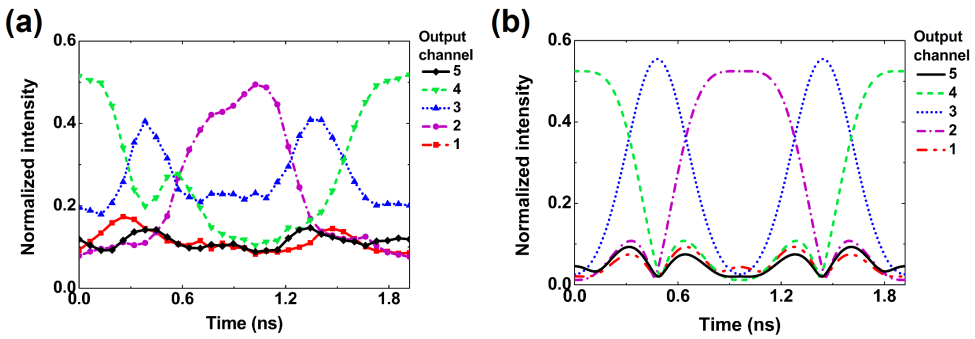

Fig. 11. (a) Time-resolved traces recorded using a MCP-PMT for the FPRs-based device for $P_{IDT} \sim 80$ mW on each IDT, measured for $\lambda = 899$ nm, and TE polarization. (b) Simulated results of the same device, assuming $\delta n_{eff} = \pm 1.50 \times 10^{-3}$, which corresponds to $\Lambda \approx \pm 1$. The access WG corresponds in both cases to i = 3. Only one acoustic period is shown.

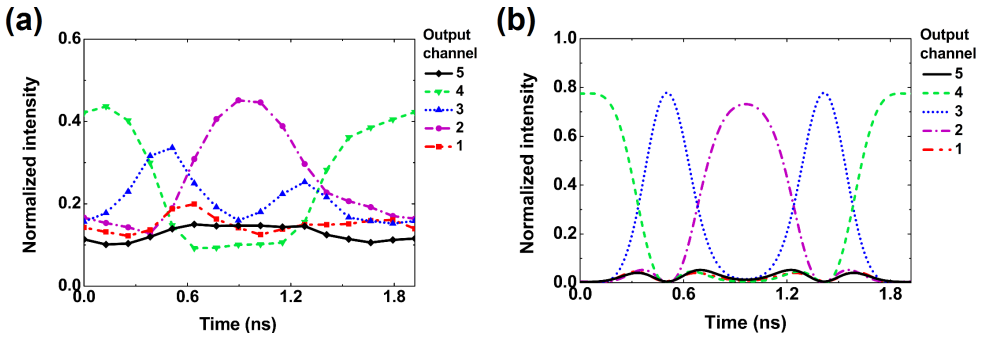

Fig. 12. (a) Time-resolved traces recorded using a MCP-PMT for the MMIs-based device corresponding to $\mathbb{S}_3''$ for $P_{IDT} \sim 80$ mW on each IDT, measured for $\lambda = 899$ nm, and TE polarization. (b) Guided-mode propagation analysis simulations of the same device, assuming $\delta n_{eff} = \pm 2.80 \times 10^{-3}$, which corresponds to $\Lambda \approx \pm 1$. The access WG corresponds in both cases to $i = 2$. Only one acoustic period is shown.

7. Conclusion

In conclusion, we have demonstrated integrated acoustically driven phased-array WDM devices that operate in the low GHz range. The two most common layouts are realized, with both free propagating regions (FPRs) and multi-mode interference (MMI) couplers being separately employed. The multiplexers operate on five equally distributed wavelength channels, with a spectral separation of 2 nm. Two interdigital transducers (IDTs) are used to create a standing SAW which modulates the effective refractive index of the arrayed WGs. Each wavelength component periodically switches paths between the preset output channel and the spectrally adjacent channels, when the proper acoustic phase is applied. Modulation times of ~ 1.9 ns have been demonstrated, with a SAW-light interaction length of ~ 120 μm, as determined by the SAW wavefront. In this way, an excellent compromise between the operation speed and the chip size is accomplished with respect to other modulation techniques. These WDM devices are suitable for applications such as a digital signal demultiplexer, or a digital channel exchanger. In general, FPRs-based WDM devices are less sensitive than MMI-based devices to the imperfections introduced during the fabrication. This makes the FPRs-based layout more convenient for applications where the crosstalk is critical. Moreover, the continuous shift of the focal point at the output coupler in the FPRs-based WDM devices makes them suitable for applications such as a multi-resolution optical spectrum analyzer. A detailed description of this device can be found in [25]. The devices were monolithically fabricated on (Al,Ga)As, and this technology can be virtually implemented in any material platform, with processing steps easily implemented in any modest cleanroom.

Acknowledgments

The authors thank W. Seidel, and S. Rauwerdink for preparation of the devices. This research has been supported by the international campus of excellence VLC/CAMPUS and by the program INNCIDE from the Spanish Ministry of Economy and Competitiveness (MINECO), through the program *"Valoritza i Transfereix"* from the Vice-Principal of Research and Scientific Policy of the Universitat de València and through the program INNOVA (grant SP20120860) from the Universitat Politècnica de València. Financial support by the Spanish MINECO Projects TEC2010-21337 and MAT2012-33483 is gratefully acknowledged. A. Crespo-Poveda and B. Gargallo acknowledge financial support through FPI grants BES-2010-036846 and BES-2011-046100, respectively.